

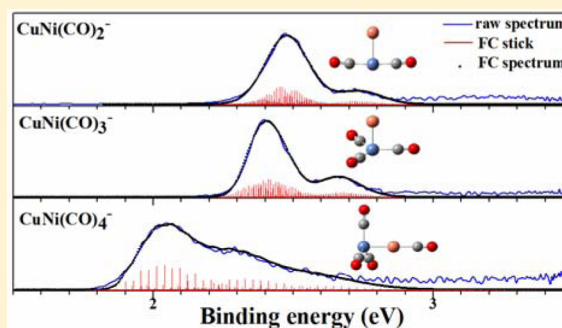
Structural Evolution of Homoleptic Heterodinuclear Copper–Nickel Carbonyl Anions Revealed Using Photoelectron Velocity-Map Imaging

Zhiling Liu, Hua Xie, Zhengbo Qin, Hongjun Fan, and Zichao Tang*

State Key Laboratory of Molecular Reaction Dynamics, Dalian Institute of Chemical Physics, Chinese Academy of Sciences, Dalian 116023, China

Supporting Information

ABSTRACT: The homoleptic heterodinuclear copper–nickel carbonyl anions $\text{CuNi}(\text{CO})_n^-$ ($n = 2-4$) were generated in a pulsed-laser vaporization source and investigated using photoelectron velocity-map imaging spectroscopy. The electron affinities of $\text{CuNi}(\text{CO})_2$ (2.15 ± 0.03 eV), $\text{CuNi}(\text{CO})_3$ (2.30 ± 0.03 eV), and $\text{CuNi}(\text{CO})_4$ (1.90 ± 0.04 eV) were deduced from the photoelectron spectra. Theoretical calculations at the B3LYP level were carried out to elucidate the structures and the electronic properties of $\text{CuNi}(\text{CO})_n^{0/1-}$ ($n = 1-4$) and to support the experimental observations. Comprehensive comparisons between experiments and calculations suggest that there is a turnover point of the absorption site during the progressive carbonylation process. The carbonyl groups are determined to be preferentially bonded to the nickel atom. When the nickel center satisfies the 18-electron configuration, the copper atom starts to adsorb additional CO molecules. These results will shed light on the bonding mechanisms of the heterometallic carbonyl clusters.



1. INTRODUCTION

Transition-metal (TM) carbonyls play an important role in catalysis and organometallic synthesis and have been studied extensively in modern coordination chemistry.¹ Gas-phase TM carbonyls are convenient models to study carbonyl chemisorption on the surface of a metal or the binding at active sites of a catalyst.¹ Thus, extensive theoretical and experimental studies on TM carbonyls have been reported in the literature, with the focus on the spectroscopic and structural properties of these complexes.² Typically, the strong bonding between a TM and CO is described with the well-documented Dewar–Chatt–Duncanson complexation model, i.e., the synergistic combination of σ donation from the filled CO σ orbital to the metal orbital and π -back-donation from the metal $d\pi$ orbital to the CO π^* orbital.³ This model has been successfully used to interpret the shifts of metal carbonyl vibrational frequencies compared to that of the free CO molecule.⁴

Among the various TM carbonyls, the nickel and copper subgroup carbonyls have drawn considerable scientific interest because of their particularly important roles in many different chemical processes, e.g., catalyst, electrocatalysis, organic synthesis, and so on.⁵ Various kinds of spectroscopic technologies have been introduced to investigate these mononuclear and homomultinuclear metal carbonyl clusters. Various charged and neutral nickel and copper carbonyls have been produced by laser vaporization in the rare gas matrices, and important information about their structures and bonding has been determined from Raman and IR spectroscopies.⁶

Collision-induced dissociation coupled with mass spectrometry has been employed to obtain the bond energies of these carbonyls.⁷ Photoelectron spectroscopy of mononuclear and dinuclear metal carbonyls has provided vibrational information and electron affinities of the corresponding ground-state neutral species.⁸ Fourier-transform microwave spectroscopy has been used to determine the molecular structures and vibrational frequencies of mononuclear monocarbonyls.⁹ Mass-selected IR photodissociation spectroscopy in the carbonyl stretching region has been devoted to the investigations on the charged TM carbonyl and their rare gas “tagged” analogues in the gas phase.¹⁰

Theoretically, a significant amount of research has been done on these carbonyls with the objective of gaining insight into the bonding mechanisms of the carbonyl group on TM clusters and explaining the experimentally observed intriguing properties of these complexes.⁷ Various density functional theory (DFT) and ab initio calculations have been performed to assist aforementioned experiments in elucidating the geometries, vibrational frequencies, dissociation energies, and electronic structures of TM carbonyls. DFT methods, both pure and hybrid, have successfully been used to examine possible structures for the mononuclear and dinuclear homoleptic TM carbonyls predicted by the 18-electron rule and to evaluate the thermochemistry for these complexes.¹¹ Polynuclear homo-

Received: May 10, 2014

Published: October 3, 2014

metallic carbonyls are also of interest for the study of the nature of metal–metal interaction and for the elucidation of factors governing the choice of a certain structural type among the numerous types (terminal, bridging, and semibridging) persistent in these compounds.¹²

However, in contrast to the vast amount of experimental and theoretical data about the versatile structural characteristics of homoleptic homonuclear TM carbonyl complexes, there is a lack of experimental research on the structural evolution for homoleptic heteronuclear TM carbonyl clusters.¹³ Heteronuclear TM carbonyls are of particular interest because of the excellent chemical reactivity of bimetallic clusters in various important processes, e.g., the chemisorption of small molecules on the alloy surface and enhancement of the catalytic effects in bimetallic nanoparticles. In doped TM clusters, the chemical activity can be tuned because the introduction of a dopant atom induces charge transfer, electronic energy level splitting, and geometric reorganization.¹⁴

Here we report our experimental and theoretical investigation on heterodinuclear copper–nickel carbonyl complexes. Note that the photoelectron spectroscopy of NiCu[−] was reported previously.¹⁵ The copper–nickel carbonyl anions CuNi(CO)_{*n*}[−] (*n* = 2–4) were produced in a pulsed-laser ablation source, and their photodetachment at 355 nm was analyzed using photoelectron velocity-map imaging spectroscopy.¹⁶ DFT calculations and Franck–Condon (FC) simulations were carried out to interpret the experimental observations. The well agreement between the experimental and simulated spectra allows the structural and spectroscopic assignments. It is found that, at the beginning of the sequential carbonylation process, the CO molecules are predicted to be preferentially bonded to the nickel atom, while the copper atom remains bare. An additional CO molecule starts to attach to the copper atom after the saturated adsorption of CO on the nickel atom.

2. EXPERIMENTAL AND THEORETICAL METHODS

2.1. Photoelectron Imaging Spectroscopy. The experiment was conducted using our collinear photoelectron velocity-map imaging spectrometer equipped with a pulsed-laser vaporization source. Details of the apparatus were described elsewhere,¹⁷ and only a brief description is presented below. CuNi(CO)_{*n*}[−] (*n* = 2–4) complexes were produced by laser vaporization of a nickel–copper alloy in the presence of a helium carrier gas seeded with 2% CO. After cooling and expansion into the source chamber, the cluster anions were extracted perpendicularly by a −1.2 kV high-pulse voltage and subjected to a Wiley–McLaren time-of-flight (TOF) mass spectrometer. The typical mass spectra of anions produced at the experimental conditions that favor the formation of clusters in the range of *m/z* 110–270 are shown in Figure 1S in the Supporting Information (SI). The assignments of each species were based on a comparison of the observed spectral pattern with the natural abundance isotopic distributions (Figure 2S in the SI, for example). Then, the anions of interest were introduced into the laser detachment region and interacted with a laser beam (355 nm from a Nd:YAG laser). The photoelectrons were extracted by a modified velocity-map imaging electrode, based on the original design of Eppink and Parker.¹⁸ After passing through a 36 cm TOF tube, the photoelectrons were mapped onto a detector consisting of a 40-mm-diameter microchannel plate assembly and a phosphor screen. The two-dimensional (2D) images on the phosphor screen were recorded by a charge-coupled-device camera. All of the raw images were reconstructed using the basis set expansion inverse Abel transform method.¹⁹ Photoelectron spectra and the photoelectron angular distribution (PAD) are obtained simultaneously by integrating the reconstructed images. The photoelectron spectra are plotted versus electron binding energy (eBE), which was obtained by subtracting the

electron kinetic energy (eKE) from the respective detachment photon energy (eBE = *hν* − eKE). The spectrometer was calibrated by the known spectrum of Cu[−].²⁰ The energy resolution is better than 50 meV at an eKE of 1 eV.

2.2. DFT Calculations. All theoretical calculations were performed using the *Gaussian 09* program package.²¹ DFT, with electron correlation effects included, appears to be a practical and effective computational tool to study TM carbonyls. The B3LYP hybrid functional, which makes use of the Hartree–Fock exact exchange and Becke’s exchange functional and Lee–Yang–Parr correlation functional,²² appears to perform well for the TM carbonyl clusters¹⁶ and thus was chosen to elucidate the electronic and geometrical structures of CuNi(CO)_{*n*}^{0/1−} (*n* = 1–4). The initial structures for heterodinuclear nickel–copper carbonyls were reasonably constructed on the basis of three different structural types of CO adsorption on the metal (terminal, symmetrically bridging, or semibridging). These candidate structures were optimized using 6-311+G* basis sets for the carbon and oxygen atoms and Stuttgart relativistic small core basis sets for the nickel and copper atoms. Singlet and triplet isomers of CuNi(CO)_{*n*}[−] (*n* = 1–4) were fully optimized in this work. However, none of the triplet isomers were found to be energetically competitive with the lowest-energy singlet isomer. Similarly, doublet and quartet isomers of CuNi(CO)_{*n*} (*n* = 1–4) were fully optimized in this work. None of the quartet isomers were found to be energetically competitive with the lowest-energy doublet isomer. Thus, for the unsaturated CuNi(CO)_{*n*} (*n* = 1–4) isomers, the lowest-lying triplet isomer lies approximately 20 kcal/mol or more in energy above the comparable lowest-lying singlet isomer. Therefore, the triplet isomers for anionic CuNi(CO)_{*n*}[−] (*n* = 1–4) and the quartet isomers for neutrals are not discussed in detail in this paper, but only the results from the global minimum and selected higher-energy isomers are presented. All of optimized ground-state and low-lying structures obtained at this step are gathered and depicted in the SI (see Figures 3S–6S).

In order to obtain better consistency with the experimental data, the ground-state and selected low-lying structures for each species were reoptimized using the Stuttgart relativistic small core basis set and efficient core potential augmented with two *f*-type and one *g*-type polarization functions for nickel [$\zeta(f) = 1.182, 4.685; \zeta(g) = 3.212$] and copper [$\zeta(f) = 1.315, 5.208; \zeta(g) = 3.665$]²³ and the aug-cc-pVTZ basis set for carbon and oxygen atoms.²⁴ Scalar (mass-velocity and Darwin) relativistic effects were taken into account via the quasi-relativistic pseudopotentials. For all calculations, the ultrafine integration grid (99590) was used to ensure the accuracy of the DFT results. Harmonic frequency calculations were performed to verify that the obtained structures are true local minima on the potential energy surfaces. The basis set superposition error²⁵ was corrected with the counterpoise method using CuNi[−] and CO molecules as fragments. The electron affinity (EA) was calculated as the difference in energy between the optimized anion and neutral species, whereas the vertical detachment energy (VDE) was calculated as the difference in energy between the anion and neutral species both computed at the anionic optimized geometry. In order to interpret the electronic and geometrical structures of CuNi(CO)_{*n*}^{0/1−} (*n* = 1–4), chemical bonding analysis and natural bonding orbital²⁶ analysis were performed on these species.

3. EXPERIMENTAL RESULTS

The photoelectron images and spectra from the detachment of CuNi(CO)_{*n*}[−] (*n* = 2–4) anions recorded at 355 nm are shown in Figure 1. The raw images (black background) collected in the experiments show the projection of the three-dimensional (3D) laboratory-frame photoelectron probability density onto the plane of the imaging detector, and the reconstructed images (purple background) represent the central slice of the 3D distribution from its 2D projection. The measured EAs, VDEs, and frequencies are summarized in Table 1, where they are compared with theoretical data at the B3LYP/Ni,Cu/Stuttgart+2f1g/C,O/aug-cc-pVTZ level of theory. Note that the experimental error bars are determined by our instrumental resolution ($\Delta E = \frac{1}{2}eKE \times 0.05$).

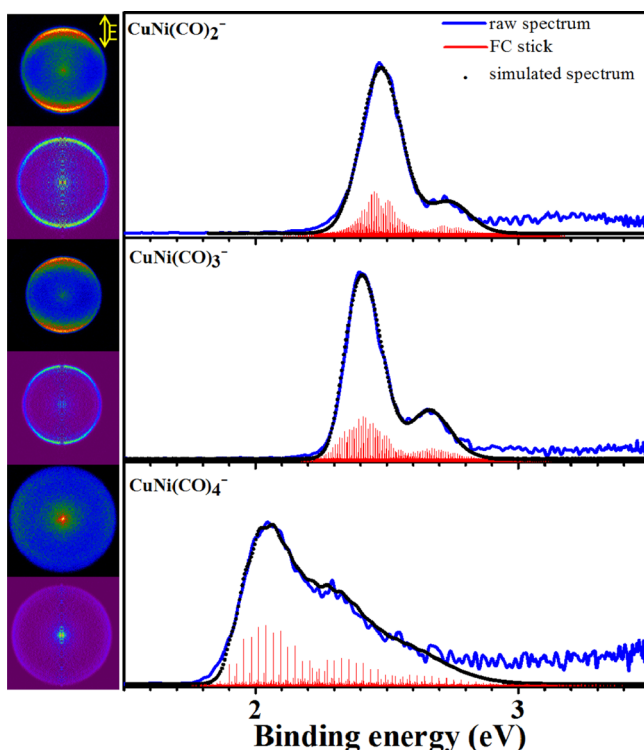


Figure 1. Photoelectron images and spectra and FC-simulated spectra for $\text{CuNi}(\text{CO})_n^-$ ($n = 2-4$) recorded at 355 nm (3.496 eV). The left side shows the raw photoelectron (black background) and reconstructed (purple background) images after inverse Abel transformation. The double arrow shows the direction of laser polarization.

The 355 nm spectra allow the ground-state transition to be observed for $\text{CuNi}(\text{CO})_n^-$ ($n = 2-4$). In these spectra, only one intense main band is revealed for each case, following by a few relatively weak sub-bands at the high-binding-energy side. The energy separations between these bands are measured to be 2016 ± 120 , 2064 ± 120 , and $2024 \pm 107 \text{ cm}^{-1}$, consistent with the vibrational frequency of the CO stretching mode, suggesting that all of these three clusters possess terminal carbonyl groups. A few lower-intensity signals revealed at the higher energy side are unresolvable because of the poor signal-to-noise ratio. The VDEs of $\text{CuNi}(\text{CO})_n^-$ ($n = 2-4$) are estimated from their well-defined band maxima to be 2.47 ± 0.03 , 2.39 ± 0.03 , and $2.05 \pm 0.04 \text{ eV}$, respectively. No vibrational structures were resolved for the broad main band in each case. On the one hand, the hot band has significant contributions to the broad bands. Our previous results on Au_4^- ,²⁷ contrasted with those reported by Wang and co-workers,²⁸ suggest that our cluster source is much “hotter”. On the other hand, a large geometry change upon photodetachment will also give rise to the electronic band spread. The broad bands prevent us from directly measuring the adiabatic detachment energies (ADEs).

To confirm the spectral assignments and gain reliable ADE values, the PESCAL program²⁹ was employed to perform FC simulations based on the results of DFT calculations. The simulated spectrum is

shown as black dots, while the solid blue curve represents the experimentally observed one. The red sticks in Figure 1 represent the relative intensities of individual vibrational transitions revealed by simulations. The simulated band origin was adjusted to give the best fit between the experimental and simulated spectra. The ADEs thus are evaluated in this way to be $2.15 \pm 0.03 \text{ eV}$ for $\text{CuNi}(\text{CO})_2^-$, $2.30 \pm 0.03 \text{ eV}$ for $\text{CuNi}(\text{CO})_3^-$, and $1.90 \pm 0.04 \text{ eV}$ for $\text{CuNi}(\text{CO})_4^-$, respectively.

Note that the spectral features of $\text{CuNi}(\text{CO})_2^-$ are quite similar to those of $\text{CuNi}(\text{CO})_3^-$ but different from those of $\text{CuNi}(\text{CO})_4^-$. Both $\text{CuNi}(\text{CO})_2^-$ and $\text{CuNi}(\text{CO})_3^-$ have similar full width at half-maxima, while the band revealed in the spectrum of $\text{CuNi}(\text{CO})_4^-$ is the broadest among the three clusters, suggesting that $\text{CuNi}(\text{CO})_4^-$ has the largest geometry change between the ground states of the anion and neutral species upon photodetachment. Additionally, VDEs are observed to decrease steadily, but not linearly, with the number of CO ligands. The VDE of the $\text{CuNi}(\text{CO})_3^-$ anion is slightly red-shifted with respect to that of $\text{CuNi}(\text{CO})_2^-$ but becomes significantly blue-shifted with respect to that of $\text{CuNi}(\text{CO})_4^-$. Figure 2 depicts the PADs

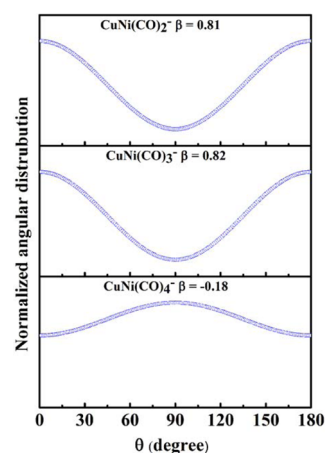


Figure 2. PADs of $\text{CuNi}(\text{CO})_n^-$ ($n = 2-4$) at 355 nm.

of $\text{CuNi}(\text{CO})_n^-$ ($n = 2-4$), normalized to 1 as the maximum intensity. Remarkably, the PAD behaviors for $\text{CuNi}(\text{CO})_2^-$ and $\text{CuNi}(\text{CO})_3^-$ differ from that of $\text{CuNi}(\text{CO})_4^-$. The anisotropy parameter (β) is 0.81 for $\text{CuNi}(\text{CO})_2^-$, 0.82 for $\text{CuNi}(\text{CO})_3^-$, and -0.18 for $\text{CuNi}(\text{CO})_4^-$. The ground-state transitions of $\text{CuNi}(\text{CO})_2^-$ and $\text{CuNi}(\text{CO})_3^-$ are parallel transitions, while $\text{CuNi}(\text{CO})_4^-$ possesses approximately vertical transition. All of these observations suggest that there is turnover point at $n = 4$ for homoleptic heterodinuclear copper–nickel carbonyl clusters $\text{CuNi}(\text{CO})_n^-$ during the sequential carbonylation process.

4. THEORETICAL RESULTS

DFT calculations were performed to elucidate the geometric and electronic structures of $\text{CuNi}(\text{CO})_n^{0/1-}$ ($n = 1-4$). For vibrational analysis, the CO frequencies at the B3LYP level are scaled by a factor of 0.971, which is the ratio of the experimental value (2143 cm^{-1}) to the B3LYP value (2207

Table 1. Calculated and Experimental EAs, VDEs, CO Stretching Vibrational Frequencies, and Anisotropy Parameters at 355 nm for Photodetachment Processes of $\text{CuNi}(\text{CO})_n^-$ ($n = 2-4$)

species	EA/eV		VDE/eV		frequency/ cm^{-1}		β
	exptl	calcd ^a	exptl	calcd ^a	exptl	calcd ^a	
$\text{CuNi}(\text{CO})_2^-$	2.15	2.04	2.47	2.39	2016	2054	0.81
$\text{CuNi}(\text{CO})_3^-$	2.30	2.34	2.39	2.51	2064	2063	0.82
$\text{CuNi}(\text{CO})_4^-$	1.90	1.99	2.05	2.28	2024	2039, 2137	-0.18

^aPredictions at the B3LYP/Ni,Cu/Stuttgart+2f1g/C,O/aug-cc-pVTZ level of theory.

cm⁻¹) of free CO. Geometry optimizations at the B3LYP level with Ni,Cu/SDD/C,O/6-311+G* basis sets were performed starting from a high number of possible candidate structures with full relaxation of all atoms. All of geometries optimized at this level are presented in Figure 3S–6S in the SI for the CuNi(CO)_n^{0/1-} (*n* = 1–4) clusters, respectively. Only the optimized global minimum and selected higher-energy isomers were further reoptimized at the B3LYP level with Ni,Cu/Stuttgart+2f1g/C,O/aug-cc-pVTZ basis sets and depicted in Figure 3. All of the vibrational frequencies of the species predicted at the B3LYP level are listed in Tables 1S–3S in the SI.

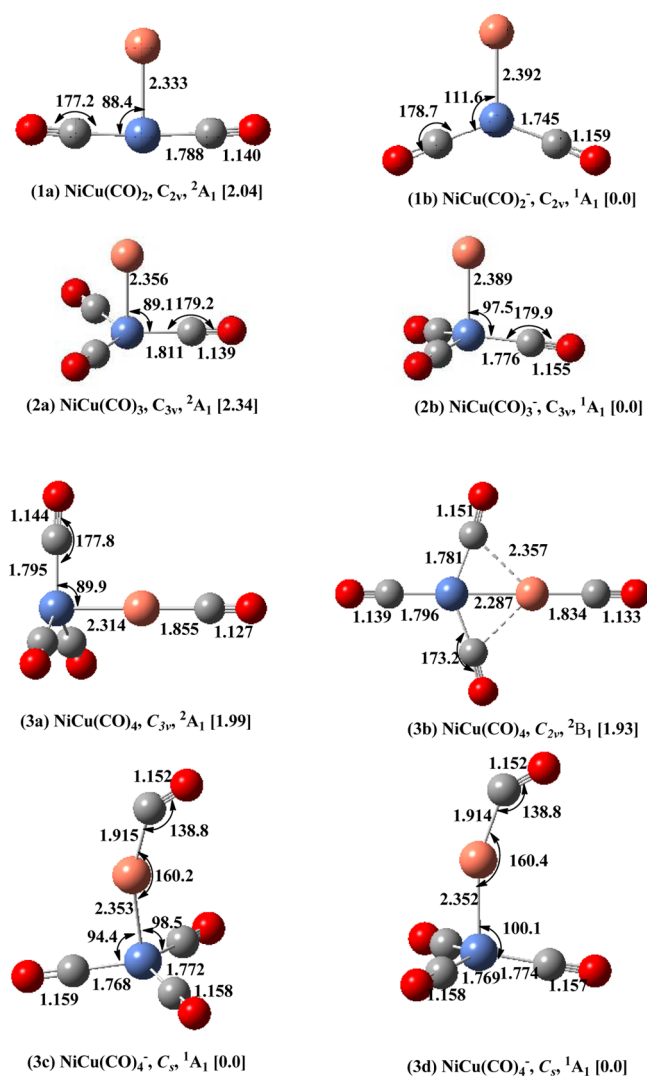


Figure 3. Optimized ground-state and selected low-lying structures of CuNi(CO)_n^{0/1-} (*n* = 2–4) at the B3LYP level. The nickel, copper, carbon, and oxygen atoms are shown in blue, brown, gray, and red, respectively. The bond lengths in angstroms and bond angles in degrees are given above the bonds, and the relative energies to the anion ground state are given in square brackets in electronvolts.

4.1. CuNiCO⁻ and CuNiCO. Our extensive geometrical optimizations (Figure 3S in the SI) for CuNiCO⁻ and CuNiCO lead to linear ground states with the carbonyl group terminally bonded to the nickel atom. Alternative optimized CuNiCO⁻ anionic structures are predicted to be at least ~0.9 eV higher in energy, hinting at the overpowering

stability of the linear structure with the carbon atom of the carbonyl group bonded to the nickel atom. For a neutral CuNiCO cluster, a low-lying linear isomer is located at 0.13 eV above the ground state, which possesses the CO molecule bonded to the copper atom. Other isomers are at least ~1.1 eV higher in energy (Figure 1S in the SI). The relative energetics of the isomers suggest that the carbonyl group prefers to be terminally bonded to the metal atom.

4.2. CuNi(CO)₂⁻ and CuNi(CO)₂. The ground-state structure for CuNi(CO)₂⁻ is Y-shaped (C_{2v}, ¹A₁), which can be viewed as a copper atom bonded to the nickel center of the bent dicarbonylnickel. Alternative optimized anionic isomers, including those with carbonyl groups bridging and terminally bonded to the copper atom, are at least ~1.0 eV above the ground state (Figure 4S in the SI). The neutral ground state (T-shaped) shows structural characteristics similar to those of the corresponding anion, except that the Ni(CO)₂ moiety is quasi-linear. The closest doublet structure, C_s (²A'), is 0.17 eV higher in energy, with one carbonyl group terminally bonded to the nickel center and the other carbonyl group bridging bonded to the nickel–copper unit. Alternative optimized neutral structures are also higher in energy (Figure 2S in the SI).

4.3. CuNi(CO)₃⁻ and CuNi(CO)₃. The ground state of CuNi(CO)₃⁻ is C_{3v} (¹A₁; Figure 3), which can be viewed as built from the tricarbonylnickel by bonding additional copper atoms on the centric nickel atom. Alternative optimized CuNi(CO)₃⁻ anion structures, including those with bridging CO and in different spin states, are at least ~1.0 eV higher in energy. The ground state for neutral CuNi(CO)₃ is umbrella-type and differs only slightly from the ground state of the anion, with three terminal carbonyl groups bending toward the copper atom.

4.4. CuNi(CO)₄⁻ and CuNi(CO)₄. The potential energy surfaces of CuNi(CO)₄⁻ and CuNi(CO)₄ are much more complicated. As shown in Figure 4S in the SI, numerous structural minima were located starting with various geometries for anionic CuNi(CO)₄⁻. Among these structures, two energetically lowest-lying isomers (3c and 3d in Figure 3) for the anionic CuNi(CO)₄⁻ show similar structural characteristics, which could be viewed as built from the C_{3v} (¹A₁) ground-state structure of the CuNi(CO)₃⁻ moiety with one more carbonyl group bonded to the copper center. These two structures were estimated to be virtually degenerate and lie significantly lower in energy than alternative optimized anionic structures, except that one possesses a staggered conformation while the other has an eclipsed conformation (the fourth carbonyl group with respect to one of three carbonyl groups in the tricarbonylnickel moiety, analogous to methanol).

A similar set of structures were optimized for the neutral CuNi(CO)₄. Two of lowest-lying structures, i.e., C_{2v} (²B₁; 3a in Figure 3) and C_{3v} (²A₁; 3b in Figure 3), are also found to be energetically degenerate, both of which are doublet states. The C_{2v} (²B₁) structure possesses two bridging carbonyl groups bonded to the Ni–Cu unit, with one terminal carbonyl bonded to the nickel center and one carbonyl group terminally bonded to the copper atom. The C_{3v} (²A₁) structure, with the nickel atom bound by three carbonyls and the copper atom bound by one carbonyl, shows structural characteristics similar to those of the corresponding anion, except the quasi-linear CuCO moiety.

5. COMPARISON BETWEEN THE EXPERIMENT AND THEORY

5.1. $\text{CuNi}(\text{CO})_2^-$. The methanal-like structure 1b with the nickel atom bound by two carbonyl groups is definitely the ground state for $\text{CuNi}(\text{CO})_2^-$, with alternative structures (Figure 4S in the SI) lying at least ~ 1.0 eV higher in energy. The predicted ground-state EA and VDE at the B3LYP level are 2.04 and 2.39 eV, which are compared to the experimental values of 2.15 and 2.47 eV, respectively. The large geometrical change from Y-shaped to T-shaped upon photodetachment is in accordance with the large difference between the calculated EA and VDE. The larger value of the experimentally measured EA relative to the predicted one at the B3LYP level indicates that the FC factor of the 0–0 transition may be negligible because of the large difference in the geometry, and the experimentally measured EA can only provide an upper limit for the true adiabatic value. Usually the totally symmetric vibrational modes may be activated upon photodetachment. Five totally symmetric vibrational modes were confirmed by our FC simulations to be activated, all of which are depicted in Figure 7S in the SI. The symmetric CO stretching vibrational frequency for $\text{CuNi}(\text{CO})_2$ is predicted by our calculation to be 2080 cm^{-1} , consistent with the revealed separation between the first and second bands in the spectrum at 355 nm.

5.2. $\text{CuNi}(\text{CO})_3^-$. The methoxyl-like structure 2b with all three carbonyls bonded to the nickel atom is clearly predicted to be the ground state for $\text{CuNi}(\text{CO})_3^-$, with alternative structures (Figure 5S in the SI) at least ~ 1.0 eV higher in energy. The EA and VDE for electron detachment from the highest occupied molecular orbital (HOMO) of $\text{CuNi}(\text{CO})_3^-$ are estimated as 2.34 and 2.51 eV (Table 1), respectively, in excellent agreement with the experimental data. Similarly, five totally symmetric vibrational modes were confirmed by our FC simulations to be activated, all of which are depicted in Figure 8S in the SI. The symmetric CO stretching vibrational frequency for $\text{CuNi}(\text{CO})_3$ is predicted as 2086 cm^{-1} , in line with the experimentally observed vibrational structure in the 355 nm spectrum of $\text{CuNi}(\text{CO})_3^-$.

5.3. $\text{CuNi}(\text{CO})_4^-$. The $\text{CuNi}(\text{CO})_4^-$ cluster is a more complicated case. As shown in Figure 3, two energetically degenerate conformational isomers (3c and 3d in Figure 3) were identified, with one being a staggered methanol-like structure and the other being an eclipsed methanol-like structure. The degenerate energetics of these structures suggests that both of them may be responsible for the experimental potential energy surfaces. These account for the broad and congested spectrum of $\text{CuNi}(\text{CO})_4^-$ at 355 nm. The Ni–Cu bonds should probably be viewed as single bonds because of the small internal rotation barrier for these unbridged structures. Similarly, two different low-lying structures (3a and 3b in Figure 3) were identified within 0.06 eV for neutral $\text{CuNi}(\text{CO})_4$, which are practically degenerate and energetically indistinguishable. The structure 3a exhibits structural characteristics similar to those of the corresponding anion, and the FC simulation based on this structure agrees well with the experimental data, reproducing the overall patterns. However, the FC factors for forming the dibridged structure 3d will be negligible, which possesses two bridging and two terminal carbonyl groups and differs distinctively from the ground state of the anion. Thus, we temporarily assign the C_{3v} (2A_1) structure as the ground state of neutral $\text{CuNi}(\text{CO})_4$. The ADE and VDE are predicted to be 1.99 and 2.28 eV,

respectively, consistent with the experimental values. The large difference between the predicted EA and VDE is consistent with the large difference in the geometry between the anion and neutral ground states. There are two potentially active totally symmetric A_1 vibrational modes involving the CO stretching, with one corresponding to the symmetric CO stretching involving the $\text{Ni}(\text{CO})_3$ moiety and the other corresponding to the CO stretching involving the CuCO moiety. On the basis of our FC simulations, the congested vibrational structure likely stems from a combination of those totally symmetric vibrational modes and the ligand bending modes, all of which are depicted in Figure 9S in the SI.

6. DISCUSSION

6.1. Structural Evolution and Sequential Carbonylation of $\text{CuNi}(\text{CO})_n^-$ ($n = 2-4$). The overall excellent agreement between the experiments and theoretical calculations lends considerable credence to the establishments of the ground-state structures for $\text{CuNi}(\text{CO})_n^-$ ($n = 2-4$). $\text{CuNi}(\text{CO})_2^-$ is found to have C_{2v} structures, in which both carbonyl groups are terminally attached to the nickel atom. The ground state of $\text{CuNi}(\text{CO})_3^-$ is favored in the tetrahedral C_{3v} structures, with all three carbonyl groups terminally bonded to the nickel center. The ground-state structure of $\text{CuNi}(\text{CO})_4^-$ could be viewed as built from the umbrella-like structure of $\text{CuNi}(\text{CO})_3$, with the copper atom bound by the additional carbonyl group. The vibrational frequencies revealed in the spectra of $\text{CuNi}(\text{CO})_n^-$ ($n = 2-4$) fall in the range of $2000-2100\text{ cm}^{-1}$, providing spectroscopic evidence of the terminal binding of CO ligands.

Comprehensive comparisons between the experiments and calculations indicate that the CO ligands are bonded unsymmetrically to the Ni–Cu unit so that the carbonyl group is preferentially bonded to the nickel atom, consistent with the very different sequential binding energies (the first three CO binding energies are 41, 47, and 28 kcal/mol for nickel^{7a} and 6, 22, and 23 kcal/mol for copper,^{30,6a} respectively). The unbridged $\text{CuNi}(\text{CO})_n$ systems can be viewed as two bonded fragments. The basic building blocks for heterodinuclear nickel–copper carbonyls are the linear $\text{Ni}(\text{CO})$ fragment, quasi-linear $\text{Ni}(\text{CO})_2$ fragment, and quasi-planar $\text{Ni}(\text{CO})_3$ fragment, as well as the bare copper atom. The ground-state structures of $\text{CuNi}(\text{CO})_n^-$ ($n = 1-3$) could be constructed by connecting a pair of these building blocks via a Ni–Cu single bond. When the nickel center satisfies the 18-electron configuration, an additional CO ligand starts to attach to the copper atom in the case of $\text{CuNi}(\text{CO})_4^-$. Thus, the lowest-lying structure for $\text{CuNi}(\text{CO})_4^-$ corresponds to a quasi-planar $\text{Ni}(\text{CO})_3$ unit bonded to a $\text{Cu}(\text{CO})$ fragment.

6.2. Comparison with Homoleptic Binuclear Carbonyl Clusters: $\text{CuNi}(\text{CO})_n$ versus $\text{Ni}_2(\text{CO})_n$ and $\text{Cu}_2(\text{CO})_n$. The distinct electronic shell structures make the nickel and copper atoms exhibit different metal–carbonyl interaction. Previous theoretical studies have proposed the different geometrical characteristics between the $\text{Ni}_2(\text{CO})_n$ and $\text{Cu}_2(\text{CO})_n$ systems.¹¹ There are many bridged global minima or low-lying structures for the $\text{Ni}_2(\text{CO})_n$ system. During the sequential carbonylation process, the first carbonyl group is attached to the nickel dimer in the bridging position between the two nickel atoms. The second carbonyl group was predicted to be terminally bonded to one of the nickel atoms in the bridged $\text{Ni}_2(\text{CO})$ fragment. The structure of $\text{Ni}_2(\text{CO})_2$ with two bridging carbonyls was predicted to be unstable. The third carbonyl group was


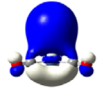

predicted to continuously terminally attach to the same nickel atom, guaranteeing this nickel atom to form a tetrahedral unit. The larger-sized $\text{Ni}_2(\text{CO})_n$ was predicted to be formed in agreement with the 18-electron rule. Their structures can be regarded as two $\text{Ni}(\text{CO})_4$ tetrahedra sharing a common face, edge, and vertex. However, the situation for $\text{Cu}_2(\text{CO})_n$ is very different. During the carbonylation process, the first three carbonyl groups were predicted to successively attach to the same copper atom. When this copper atom is saturated with CO, an additional CO ligand starts to terminally attach to another copper atom.

The $\text{CuNi}(\text{CO})_n$ system, a class of heterodinuclear carbonyls with significantly geometrical characteristics, is structurally analogous to $\text{Cu}_2(\text{CO})_n$. The very different binding energies make the carbonyl preferentially adsorb onto the nickel atom. The difficulty of breaking the filled d^{10} shell of the copper atom impedes the bridged adsorption of CO on the NiCu unit. Thus, for the cases of $\text{CuNi}(\text{CO})_n$ ($n = 1-3$), the carbonyl groups are terminally attached to the nickel center. Provided that the copper atom is viewed as a ligand, the nickel in $\text{CuNi}(\text{CO})_3^-$ is saturated and satisfies the 18-electron rule. The additional carbonyl group starts to be bonded to the copper center at $n = 4$. Hence, the evolution from CuNiCO to $\text{CuNi}(\text{CO})_4$ may even be deemed to be molecular models for qualitatively understanding of the initially sequential CO adsorption on nickel-copper alloy surfaces.

6.3. Chemical Bonding in $\text{CuNi}(\text{CO})_n^-$ and $\text{CuNi}(\text{CO})_n$ ($n = 2-4$). Typically, the strong chemical bonding between TM and carbonyl groups arises from the synergistic σ -donation and π -back-donation interactions. The molecular orbitals (MOs) of $\text{CuNi}(\text{CO})_n$ ($n = 2-4$; Figures 10S–12S in the SI) allow a qualitative understanding of this scheme. HOMO–8 and HOMO–9 of $\text{CuNi}(\text{CO})_2$, HOMO–4 and HOMO–5 of $\text{CuNi}(\text{CO})_3$, and HOMO–1 and HOMO–2 of $\text{CuNi}(\text{CO})_4$ account for the Ni–CO π -back-donation interactions. Owing to contraction of the metal 3d orbital with the atomic number, back-donation from the Cu 3d orbitals into $p\pi^*(\text{CO})$ will be less important than that for the nickel.^{11b} The preference of CO binding to nickel over copper can be attributed to weaker bonding interaction between copper and CO because of the lack of π back-donation. As can be seen from HOMO–9 in Figure 10S in the SI and from HOMO–5 in Figure 11S in the SI, the linearization or planarization of $\text{Ni}(\text{CO})_n$ fragments will benefit for the 3d of copper overlapping with the 3d of nickel, thus participating in π back-donation. The peculiar $3d^{10}4s^1$ shell of a copper atom endows it with pseudohalogenic nature. The Cu^- ion can be viewed as a pseudohalogenic ligand bonded to nickel. The charge distribution (Table 2) reveals that both the copper center and carbonyl groups in anionic $\text{CuNi}(\text{CO})_n^-$ possess a considerable amount of negative charge, causing significant repulsion between them. The repulsion is decreased by the carbonyl groups bending toward the opposite of the copper atom, thus endowing the anions with a Y-shaped or inverted-umbrella-like characteristic. The large structural change between the anionic and neutral species consists of the broad spectral features in Figure 1.

The VDEs in the $\text{CuNi}(\text{CO})_n^-$ ($n = 2-4$) series are somewhat higher than that of the bare CuNi^- , exhibiting a monotonic decrease as a function of CO, 2.47 eV for $\text{CuNi}(\text{CO})_2^-$, 2.39 eV for $\text{CuNi}(\text{CO})_3^-$, and 2.05 eV for $\text{CuNi}(\text{CO})_4^-$. This trend is consistent with previous investigations on the other unsaturated metal carbonyl clusters, indicating a sequential carbonylation of the metal cluster.^{8b} The

Table 2. Contribution (%) of the Ni 4p, Cu 4s, and CO $p\pi^*$ Components of CO Ligands in the HOMOs of $\text{CuNi}(\text{CO})_n^-$ ($n = 2-4$)

species	HOMO	Cu 4s	CO $p\pi^*$	Ni 4p	Mulliken charge		
					Cu	Ni	per CO
$\text{CuNi}(\text{CO})_2^-$		62%	16%	16%	-0.37	0.96	-0.79
$\text{CuNi}(\text{CO})_3^-$		48%	25%	21%	-0.41	1.21	-0.60
$\text{CuNi}(\text{CO})_4^-$		20%	47%	25%	-0.70	1.02	-0.51

electron-donor capability of CO is deemed to decrease the electron binding energies of TM carbonyls. The VDE trend is related to the nature of the HOMO and can be seen more clearly from the HOMO pictures, as shown in Table 2. MO analyses show that the HOMOs of $\text{CuNi}(\text{CO})_n^-$ consist mainly of 4s of the copper atom and $p\pi^*$ of the CO ligands, as well as the contribution from 4p of the nickel atom. Electronic delocalization among the metal and CO ligands will promote the electron binding energies, compared to the bare metal clusters. However, the corresponding component contributed from the CO ligands is antibonding. Removal of an electron from these MOs will give rise to the shortening of the bond lengths of C–O and the activation of the CO stretching vibration, as a result of the weakening of the antibonding interaction between carbon and oxygen. Furthermore, the contribution of $p\pi^*$ components of CO ligands exhibits an increase as a function of CO during the sequential carbonylation process, consistent with the monotonic decrease of VDEs.

The angular distributions from imaging also reveal important electronic structure information on the $\text{CuNi}(\text{CO})_n^-$ ($n = 2-4$) series and the nature of the orbitals from which the electron is removed. For the spectral peaks in the imaging of $\text{CuNi}(\text{CO})_2^-$ and $\text{CuNi}(\text{CO})_3^-$, the photoelectron intensity is more intense in the direction parallel to laser polarization, corresponding to a p wave. For the case of the $\text{CuNi}(\text{CO})_4^-$ anion, the distribution peaks at $\theta = 90^\circ$, completely opposite to the PAD behaviors of $\text{CuNi}(\text{CO})_2^-$ and $\text{CuNi}(\text{CO})_3^-$. The transformation of the angular distributions is consistent with variation of the contributions of Cu 4s, Ni 4p, and CO $p\pi^*$ in the HOMOs. Initially, the contribution from Cu 4s is predominant, giving rise to more parallel angular distributions. With an increase of the p components, the s + d wave contributes more and interferes with the p wave, resulting in slightly perpendicular angular distributions.

7. CONCLUSIONS

Photoelectron velocity-map spectroscopy combined with DFT calculations is performed to probe the structural evolution of gaseous $\text{CuNi}(\text{CO})_n^-$ ($n = 2-4$) and their electronic structures. The consistence between the experimental and theoretical calculations and FC simulations indicates that CO is preferentially attached to the nickel atom so that the CO ligands are bonded unsymmetrically to the Ni–Cu unit, and the crossover point of the absorption site occurs at $n = 4$. The

anionic and neutral $\text{CuNi}(\text{CO})_2$ possess Y-shaped and T-shaped structures with two CO ligands bonded to the nickel center, respectively. The anionic and neutral $\text{CuNi}(\text{CO})_3$ exhibit umbrella-like and inverted-umbrella-like structural characteristics, respectively, with all three carbonyl groups terminally bonded to the nickel center. The $\text{CuNi}(\text{CO})_4$ complex can be viewed as built from $\text{CuNi}(\text{CO})_3$ with one more carbonyl group bonded to the copper atom. The $\text{CuNi}(\text{CO})_n$ system investigated in the current work will benefit from the qualitative understanding of CO adsorption on nickel–copper alloy surfaces.

■ ASSOCIATED CONTENT

■ Supporting Information

Complete ref 21, mass spectra, comparison of the spectral pattern of the $\text{CuNi}(\text{CO})_3^-$ anion with the natural abundance isotopic distributions, optimized ground states and low-lying isomers, predicted harmonic vibrational frequencies for neutral and anionic $\text{CuNi}(\text{CO})_n$ ($n = 1-4$), and the MOs at the B3LYP level. This material is available free of charge via the Internet at <http://pubs.acs.org>.

■ AUTHOR INFORMATION

Corresponding Author

*E-mail: zctang@dicp.ac.cn. Tel.: +86-411-84379365. Fax: +86-411-84675584.

Notes

The authors declare no competing financial interest.

■ ACKNOWLEDGMENTS

This work was supported by the National Natural Science Foundation of China (Grants 21103186 and 21273233), the Ministry of Science and Technology of China, and the Chinese Academy of Sciences.

■ REFERENCES

- (1) Somorjai, G. A.; Li, Y. M. *Introduction to Surface Chemistry and Catalysis*, 2nd ed.; John Wiley & Sons: New York, 2010.
- (2) Zhou, M. F.; Andrews, L.; Bauschlicher, C. W. *Chem. Rev.* **2001**, *101* (7), 1931–1962.
- (3) (a) Chatt, J.; Duncanson, L. A. *J. Chem. Soc.* **1953**, 2939–2947. (b) Chatt, J.; Duncanson, L. A.; Venanzi, L. M. *J. Chem. Soc.* **1955**, 4456–4460. (c) Chatt, J.; Guy, R. G.; Duncanson, L. A. *J. Chem. Soc.* **1961**, 827–834.
- (4) Ricks, A. M.; Reed, Z. E.; Duncan, M. A. *J. Mol. Spectrosc.* **2011**, *266* (2), 63–74.
- (5) Cotton, F. A.; Wilkinson, G.; Murillo, C. A.; Bochmann, M. *Advanced Inorganic Chemistry*, 6th ed.; John Wiley: New York, 1999.
- (6) (a) Zhou, M. F.; Andrews, L. *J. Chem. Phys.* **1999**, *111* (10), 4548–4557. (b) Liang, B. Y.; Zhou, M. F.; Andrews, L. *J. Phys. Chem. A* **2000**, *104* (17), 3905–3914. (c) Jiang, L.; Xu, Q. *J. Phys. Chem. A* **2005**, *109* (6), 1026–1032. (d) Jiang, L.; Xu, Q. *J. Phys. Chem. A* **2006**, *110* (40), 11488–11493. (e) Xu, Q.; Jiang, L. *J. Phys. Chem. A* **2006**, *110* (8), 2655–2662. (f) Jiang, L.; Xu, Q. *J. Chem. Phys.* **2008**, *128* (12), 124317.
- (7) (a) Sunderlin, L. S.; Wang, D.; Squires, R. R. *J. Am. Chem. Soc.* **1992**, *114* (8), 2788–2796. (b) Grushow, A.; Ervin, K. M. *J. Am. Chem. Soc.* **1995**, *117* (46), 11612–11613. (c) Meyer, F.; Chen, Y.-M.; Armentrout, P. B. *J. Am. Chem. Soc.* **1995**, *117* (14), 4071–4081. (d) Spasov, V. A.; Lee, T.-H.; Ervin, K. M. *J. Chem. Phys.* **2000**, *112* (4), 1713–1720. (e) Zhang, X. G.; Armentrout, P. B. *Organometallics* **2001**, *20* (20), 4266–4273.
- (8) (a) Reutt, J. E.; Wang, L. S.; Lee, Y. T.; Shirley, D. A. *Chem. Phys. Lett.* **1986**, *126* (5), 399–404. (b) Zhai, H. J.; Kiran, B.; Dai, B.; Li, J.; Wang, L. S.; Unique, C. O. *J. Am. Chem. Soc.* **2005**, *127* (34), 12098–

12106. (c) Stanzel, J.; Aziz, E. F.; Neeb, M.; Eberhardt, W. *Collect. Czech. Chem. Commun.* **2007**, *72* (1), 1–14. (d) Zhai, H. J.; Pan, L. L.; Dai, B.; Kiran, B.; Li, J.; Wang, L. S. *J. Phys. Chem. C* **2008**, *112* (31), 11920–11928. (e) Wang, Y. L.; Zhai, H. J.; Xu, L.; Li, J.; Wang, L. S. *J. Phys. Chem. A* **2010**, *114* (3), 1247–1254. (f) Pal, R.; Huang, W.; Wang, Y. L.; Hu, H. S.; Bulusu, S.; Xiong, X. G.; Li, J.; Wang, L. S.; Zeng, X. C. *J. Phys. Chem. Lett.* **2011**, *2* (18), 2288–2293.

(9) (a) Evans, C. J.; Gerry, M. C. L. *J. Phys. Chem. A* **2001**, *105* (42), 9659–9663. (b) Yamazaki, E.; Okabayashi, T.; Tanimoto, M. *Chem. Phys. Lett.* **2004**, *396* (1–3), 150–154. (c) Okabayashi, T.; Yamamoto, T.; Okabayashi, E. Y.; Tanimoto, M. *J. Phys. Chem. A* **2011**, *115* (10), 1869–1877.

(10) (a) Velasquez, J.; Duncan, M. A. *Chem. Phys. Lett.* **2008**, *461* (1–3), 28–32. (b) Velasquez, J.; Njegic, B.; Gordon, M. S.; Duncan, M. A. *J. Phys. Chem. A* **2008**, *112* (9), 1907–1913. (c) Brathwaite, A. D.; Reed, Z. D.; Duncan, M. A. *J. Phys. Chem. A* **2011**, *115* (38), 10461–10469. (d) Chi, C. X.; Cui, J. M.; Xing, X. P.; Wang, G. J.; Liu, Z. P.; Zhou, M. F. *Chem. Phys. Lett.* **2012**, *542* (0), 33–36. (e) Cui, J. M.; Xing, X. P.; Chi, C. X.; Wang, G. J.; Liu, Z. P.; Zhou, M. F. *Chin. J. Chem.* **2012**, *30* (9), 2131–2137. (f) Cui, J. M.; Wang, G. J.; Zhou, X. J.; Chi, C. X.; Hua, L. Z.; Liu, Z. P.; Zhou, M. F. *Phys. Chem. Chem. Phys.* **2013**, *15* (25), 10224–10232. (g) Cui, J. M.; Zhou, X. J.; Wang, G. J.; Chi, C. X.; Liu, Z. P.; Zhou, M. F. *J. Phys. Chem. A* **2013**, *117* (33), 7810–7817.

(11) (a) Ignatyev, I. S.; Schaefer, H. F., III; King, R. B.; Brown, S. T. *J. Am. Chem. Soc.* **2000**, *122* (9), 1989–1994. (b) Li, Q. S.; Liu, Y. D.; Xie, Y. M.; King, R. B.; Schaefer, H. F. *Inorg. Chem.* **2001**, *40* (23), 5842–5850.

(12) (a) Xie, Y. M.; Schaefer, H. F., III; King, R. B. *J. Am. Chem. Soc.* **2000**, *122* (36), 8746–8761. (b) Wang, H. Y.; Xie, Y. M.; King, R. B.; Schaefer, H. F., III. *J. Am. Chem. Soc.* **2006**, *128* (35), 11376–11384.

(13) (a) Araki, M.; Ponc, V. *J. Catal.* **1976**, *44* (3), 439–448. (b) De Haeck, J.; Veldeman, N.; Claes, P.; Janssens, E.; Andersson, M.; Lievens, P. *J. Phys. Chem. A* **2011**, *115* (11), 2103–2109.

(14) (a) Neukermans, S.; Janssens, E.; Tanaka, H.; Silverans, R. E.; Lievens, P. *Phys. Rev. Lett.* **2003**, *90* (3), 033401. (b) Dong, L. H.; Yin, B.; Zhang, L.; Yin, Y. S.; Zhang, Y. J. *Synth. Met.* **2012**, *162* (1–2), 119–125.

(15) Dixon-Warren, S. J.; Gunion, R. F.; Lineberger, W. C. *J. Chem. Phys.* **1996**, *104* (13), 4902–4910.

(16) Liu, Z. L.; Xie, H.; Qin, Z. B.; Cong, R.; Wu, X.; Tang, Z. C.; Lu, X.; He, J. *J. Chem. Phys.* **2012**, *137* (20), 204302.

(17) Wu, X.; Qin, Z. B.; Xie, H.; Wu, X. H.; Cong, R.; Tang, Z. C. *Chin. J. Chem. Phys.* **2010**, *23* (4), 373.

(18) Eppink, A. T. J. B.; Parker, D. H. *Rev. Sci. Instrum.* **1997**, *68* (9), 3477–3484.

(19) Dribinski, V.; Ossadtchi, A.; Mandelshtam, V. A.; Reisler, H. *Rev. Sci. Instrum.* **2002**, *73* (7), 2634–2642.

(20) (a) Ho, J.; Ervin, K. M.; Lineberger, W. C. *J. Chem. Phys.* **1990**, *93* (10), 6987–7002. (b) Taylor, K. J.; Pettiette-Hall, C. L.; Cheshnovsky, O.; Smalley, R. E. *J. Chem. Phys.* **1992**, *96* (4), 3319–3329.

(21) Frisch, M. J.; et al. *Gaussian 09*, revision A.02; Gaussian, Inc.: Wallingford, CT, 2009.

(22) (a) Lee, C.; Yang, W.; Parr, R. G. *Phys. Rev. B* **1988**, *37* (2), 785–789. (b) Becke, A. D. *J. Chem. Phys.* **1993**, *98* (7), 5648–5652.

(c) Stephens, P. J.; Devlin, F. J.; Chabalowski, C. F.; Frisch, M. J. *J. Phys. Chem.* **1994**, *98* (45), 11623–11627.

(23) Martin, J. M. L.; Sundermann, A. *J. Chem. Phys.* **2001**, *114* (8), 3408–3420.

(24) Dunning, T. H. *J. Chem. Phys.* **1989**, *90* (2), 1007–1023.

(25) Boys, S. F.; Bernardi, F. *Mol. Phys.* **1970**, *19* (4), 553–566.

(26) Reed, A. E.; Curtiss, L. A.; Weinhold, F. *Chem. Rev.* **1988**, *88* (6), 899–926.

(27) Liu, Z. L.; Qin, Z. B.; Xie, H.; Cong, R.; Wu, X.; Tang, Z. C. *J. Chem. Phys.* **2013**, *139* (9), 094306.

(28) Yang, Z.; Leon, I.; Wang, L. S. *J. Chem. Phys.* **2013**, *139* (2), 021106.

(29) Ervin, K. M. *PESCAL*, 2010, webpage at <http://wolfweb.unr.edu/~ervin/pes/>.

(30) Blitz, M. A.; Mitchell, S. A.; Hackett, P. A. J. *Phys. Chem.* **1991**, 95 (22), 8719–8726.